Laser-driven shock waves studied by x-ray radiography

L. Antonelli,[*] S. Atzeni, and A. Schiavi

Dipartimento SBAI, Università degli Studi di Roma "La Sapienza," Via Antonio Scarpa 14, 00161 Roma, Italy

S. D. Baton, E. Brambrink, and M. Koenig

Laboratoire LULI, Ecole Polytechnique, 91128 Palaiseau Cedex, France

C. Rousseaux

CEA, DAM, DIF, 91297 Arpajon, France

M. Richetta

Dipartimento di Ingegneria Industriale, Università degli Studi di Roma "Tor Vergata," Via del Politecnico 1, 00133 Roma, Italy

D. Batani, P. Forestier-Colleoni, E. Le Bel, Y. Maheut, T. Nguyen-Bui, X. Ribeyre, and J. Trela

Université de Bordeaux, CNRS, CEA, CELIA, UMR 5107, 33405 Talence, France

Multimegabar laser-driven shock waves are unique tools for studying matter under extreme conditions. Accurate characterization of shocked matter is for instance necessary for measurements of equation of state data or opacities. This paper reports experiments performed at the LULI facility on the diagnosis of shock waves, using x-ray-absorption radiography. Radiographs are analyzed using standard Abel inversion. In addition, synthetic radiographs, which also take into account the finite size of the x-ray source, are generated using density maps produced by hydrodynamic simulations. Reported data refer to both plane cylindrical targets and hemispherical targets. Evolution and deformation of the shock front could be followed using hydrodynamic simulations.

I. INTRODUCTION

The generation of multimegabar shock waves in the interaction of high-power lasers with solid matter [1–4] allows studies of matter at extreme conditions [5,6]. In particular, we refer to the so-called warm dense matter and hot dense matter, relevant to astrophysics, material science, and inertial confinement fusion [7,8]. The strongly coupled and degenerate states of matter in those conditions make their description far from ideal. In order to discriminate between different theoretical models, accurate measurements are needed.

Most of the available large-scale facilities allow one to study compression in plane geometry only. However, high pressure in plane geometry with a laser of moderate pulse energy (less than 1 kJ) requires a small focal spot to maximize the intensity on target and this leads to two-dimensional (2D) effects and lateral dispersion of the energy during the propagation of the shock wave over distances comparable to or longer than the focal spot size. The nonuniformity of the shock front hinders accurate shock diagnosis. In this context, we performed an experiment at the LULI laser facility aiming at the accurate detection of shape and position of a strong laser-driven shock wave. We examined two different laser-target configurations. In the first one we irradiated a plane surface and in the second one a hemisphere. We used two-dimensional x-ray absorption radiography to obtain an image of the shocked target and in particular of the shock wave front. This technique was already used in the past at the same laser facility [9–13] and elsewhere (e.g., [14,15]). Streaked radiography (i.e., time-resolved one-

dimensional radiography) is also used to measure converging shock speed in spherical targets [16,17].

In our work we also developed a specific postprocessing module coupled to the hydrodynamic code DUED [18], which allows us to compare directly the experimental results with the numerical density maps. The module calculates a synthetic radiograph taking into account the finite x-ray source dimensions and its spatial distribution, which can play a non-negligible role. Indeed, the standard Abel inversion method (which relies on the plane wave front) cannot take into account the spatial properties of the backlighting source. The Abel inversion of experimental data is also intrinsically noisy due its mathematical formulation. Therefore, it requires a fitting and filtering procedure, which can wipe out a significant amount of information contained in experimental data. We show instead that with our approach we can obtain a satisfactory reproduction of experimental data.

II. EXPERIMENTAL SETUP

The experimental setup is represented in Fig. 1. The laser pulse of LULI2000 was focused on a CH plastic target to generate a strong shock wave that was characterized using x-ray-absorption radiography. X rays were generated by a vanadium backlighter irradiated by the PICO2000 laser.

A. Laser

LULI2000 is a Nd:glass laser delivering up to 500 J in the second harmonic ($2\omega = 526$ nm) in 2 ns with a flat-top temporal profile (see Sec. III for details). The PICO2000

———————
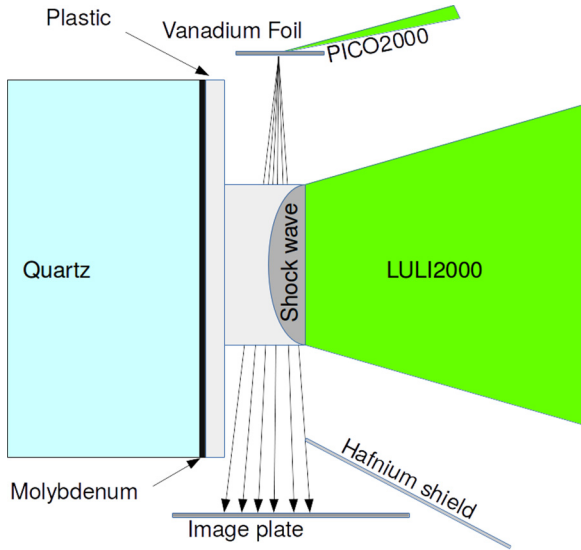[*]luca.antonelli@uniroma1.it; luca.antonelli.1985@gmail.com

FIG. 1. Sketch of the experimental setup.

Nd:glass laser can deliver up to 40 J in the second harmonic ($2\omega = 526$ nm) with a Gaussian pulse duration of about 3 ps.

The LULI2000 nanosecond laser pulse was focused using a random phase plate, producing a nominal Gaussian focal spot with a 330-μm FWHM. The resulting intensity on target was on the order of 10^{14} W cm^{-2}. However, the actual laser spot, measured using a different cw laser, varied significantly from shot to shot and was typically smaller than the nominal one. Also, it showed significant departures from cylindrical symmetry. In the simulations presented in the following we assume a (cylindrically symmetrical) Gaussian focal spot with a 200-μm FWHM.

B. Targets

Two different layered targets were used, as depicted in Figs. 2(a) and 2(b). Both targets had a front plastic layer (polypropylene) for laser interaction and shock wave propagation with two different shapes: a cylinder with a radius of 250 μm and length of 250 μm [Fig. 2(a)] and a half sphere with radius of 250 μm [Fig. 2(b)]. A middle layer of 15 μm
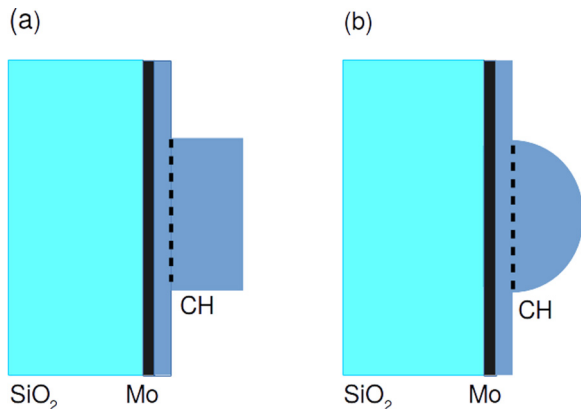

FIG. 2. (a) Cylindrical target with a flat interaction surface and (b) hemispherical target.
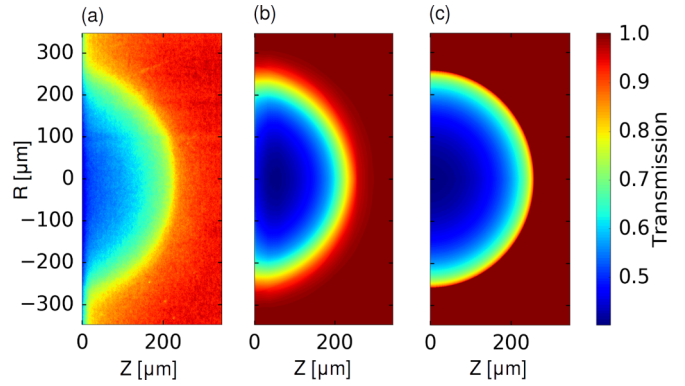

FIG. 3. (a) Radiography test of a hemispherical target, compared with (b) a synthetic radiograph and (c) the Abel transform of the numerical density map.

molybdenum was used to shield the streak cameras [for a velocity interferometer system for any reflector (VISAR) [19] and streaked optical pyrometry (SOP) [1]] from direct laser illumination. Also it was intended to mitigate the preheating of the material ahead the shock due to x rays and hot electrons. A layer of quartz was used to measure the shock velocity using a VISAR [6]; VISAR measurements are not discussed in this paper.

C. X-ray radiography

The main diagnostic technique was x-ray-absorption radiography. The PICO2000 beam was focused onto a 10-μm-thick vanadium foil to produce an intense x-ray pulse. The interaction between the intense laser beam and the target generates hot electrons, which excite the inner-shell electrons of vanadium producing K_α radiation, with energy of 4.9 keV. We recorded this K_α radiation using a germanium crystal in a von Hamos configuration [20,21]. To record the radiograph we used an image plate placed 28 cm away from the target. The distance between the x-ray source and the target was 0.8 cm. The expected magnification was therefore 35 times. The x-ray-absorption setup was tested by irradiating a hemispherical target with radius of 250 μm (see Fig. 3 and the discussion in the next section). The synchronization between LULI2000 and PICO2000 had a jitter of 100 ps.

Data treatment and analysis

Radiography generates a map of x-ray transmission (ratio of transmitted intensity to incident intensity) through the target. Using this information, one can reconstruct the density map of the target under certain conditions [22]. Assuming cylindrical geometry, the incident x-ray intensity $I(y,z)$ (with z the target symmetry axis and y the distance from it in the experimental image) is described by

$$I(y,z) = I_0 \exp\left(-\int_{-x_0}^{+x_0} k(E,x,y,z)dx\right), \quad (1)$$

where I_0 is the backlighter intensity (in the experiment obtained for each radiograph from the unattenuated x-ray signal). The attenuation coefficient k depends on the x-ray

energy E and material according to

$$k(E,x,y,z) = \mu(E,x,y,z)\rho(x,y,z), \qquad (2)$$

where μ is the mass attenuation coefficient characteristic of the specific material and ρ is the material density. We can then calculate

$$-\ln\left(\frac{I}{I_0}\right) = 2\int_0^{+x_0} k(E,x,y,z)dx. \qquad (3)$$

Changing the variable from x to r, $x = \sqrt{r^2 - y^2}$, we finally have

$$-\ln\left(\frac{I}{I_0}\right) = 2\int_y^{+\infty} \frac{k(E,r,z)r\,dr}{\sqrt{r^2 - y^2}}. \qquad (4)$$

We can apply Abel inversion to obtain the attenuation coefficient from Eq. (4), which gives

$$k(E,r,z) = \frac{1}{\pi}\int_r^{+\infty} \frac{d}{dx}\left[\ln\left(\frac{I(y,z)}{I_0}\right)\right] \frac{dy}{\sqrt{y^2 - r^2}}, \qquad (5)$$

where r is the distance of the point of the image from the symmetry axis z in the inverted image. Due to the assumption of cylindrical symmetry, only half of the image is actually used in the inversion process. Assuming a mass attenuation coefficient μ depending only on the x-ray energy (which is appropriate in the range of density and temperature considered in our experiment [22]), one can obtain the density map of the target from Eq. (2). In our case (for 4.9-keV photons in plastic) $\mu \approx 18.5$ cm^2/g [23]. We developed a program to compute the *Abel inversion* of the experimental transmission map to retrieve the density map. We also developed a module that computes the *Abel transform* to obtain a transmission map from a given density map.

In addition, we produced numerical density maps, which can be compared with experimental data. We used the 2D, two-temperature radiation hydrodynamic code DUED. Equation of state (EOS) data are provided by a slightly improved version of the model of Ref. [24]. We have checked that DUED with the quoted EOS reproduces with high accuracy the experimental data [25] for plastic at pressures in the range 1–10 Mbars. Radiative transfer is described by a multigroup diffusion scheme. Opacities are provided by an upgraded version of the SNOP code [26]. While the original SNOP code only applies to single-element materials, the present version also deals with mixtures. Moreover, we developed a module that can calculate a synthetic radiograph using the numerical density map. In this way we were able to include important source properties such as the finite width of the x-ray source that cannot be included in a simple Abel treatment.

The whole procedure was tested in the case of the nonirradiated hemispherical target. Figure 3 shows the experimental radiograph [Fig. 3(a)], the synthetic radiograph [Fig. 3(b)], and the Abel transform [Fig. 3(c)]. Figure 4 shows transmission vs the axial coordinate z, as obtained from the experimental radiograph, the synthetic radiograph, and the Abel transform. The error bars are estimated from the fluctuations of the backlighting source, which gives the dominant contribution to the noise. In the synthetic radiograph an x-ray source with Gaussian intensity distribution and a 30-μm FWHM was assumed. Such a value of the K_α source size is larger than
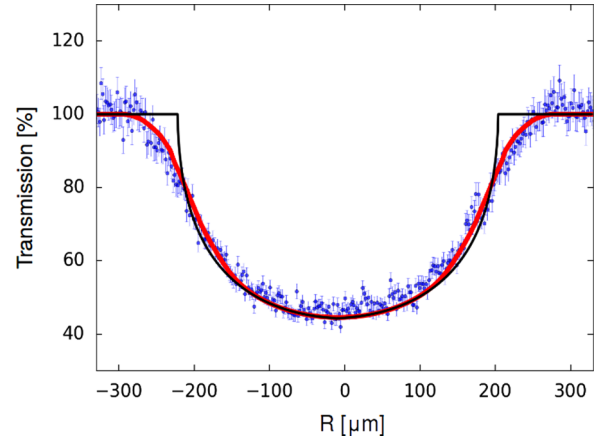

FIG. 4. Transmission of the hemispherical target along the line $z = 130$ μm. The experimental result (dots) is compared with the synthetic radiograph (red curve) and the Abel transform of the numerical density map (black curve).

the laser spot size, as reported in previous experiments [27]. Figure 4 shows how the source width plays a fundamental role. Unlike the experimental data, the Abel transform shows a sharp edge at the target border and underestimates transmission. The effect of the x-ray source size will be discussed in more detail in Sec. III A.

III. RESULTS

We applied our simulation-assisted radiography technique to the data collected in the experiment for the cylindrical target and then for the hemispherical target. The raw data for both targets are shown in Fig. 5. Notice that all images are not symmetrical with respect to the z axis. In the case of hemispherical targets, in addition, the shock front is clearly slightly tilted with respect to the same axis. Since our procedure requires cylindrical symmetry, we rotated these images. In all cases, we used half an image (the upper portion). We checked that using the lower portion leads to similar results.

A. Cylindrical target

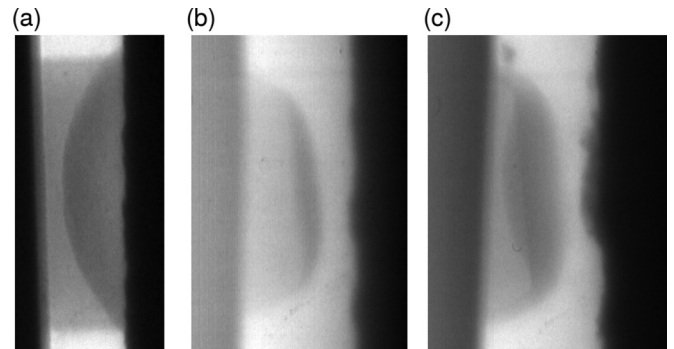We consider a shot in which the laser delivered 400 J in the second harmonic with a flat top of 1.2 ns, preceded by

FIG. 5. Experimental radiographs: (a) cylindrical target at $t = 4.7$ ns and (b) and (c) spherical target at $t = 2.7$ ns and $t = 4.7$ ns, respectively.
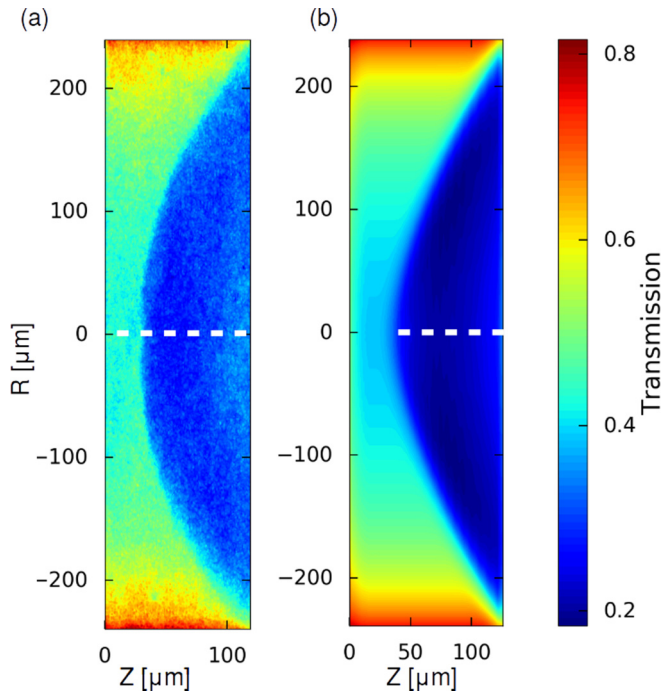
(a)

(b)

FIG. 6. Shock wave in the cylindrical target: (a) experimental radiograph and (b) synthetic radiograph. The laser pulse driving the shock comes from the right-hand side.
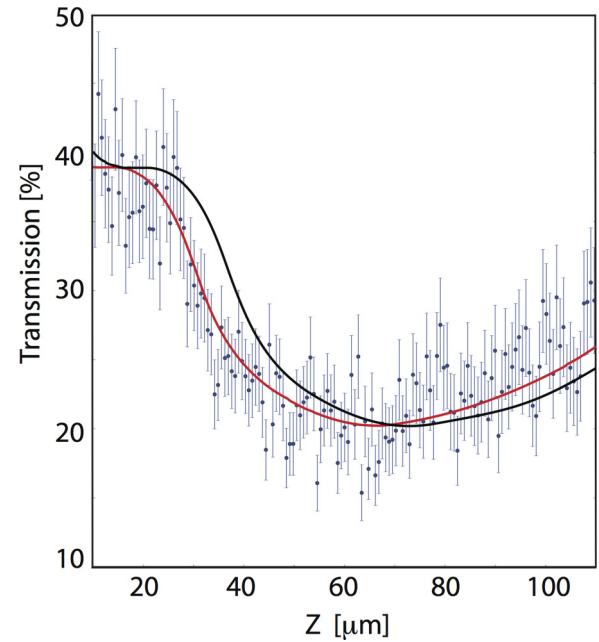

FIG. 7. Cylindrical target. Experimental transmission (dots, with error bars) and simulated transmission (black curve). The red curve is the simulated transmission curve shifted 7 μm to the left.

a linear rise in 0.4 ns and followed by a linear decrease in 1.2 ns. The picosecond pulse was delayed by 4.7 ns from the start time of the nanosecond pulse. Figure 6 shows the experimental radiograph [Fig. 6(a)] together with the synthetic radiograph [Fig. 6(b)]. The synthetic radiograph was generated by postprocessing a DUED hydrodynamic simulation, using nominal laser power (and hence energy), and a Gaussian focal spot with a 200-μm FWHM. A comparison of Figs. 6(a) and 6(b) shows good general agreement. Notice, however, that the experimental image is not exactly symmetric; also, the curvature of the shock front in the two images is slightly different. The experimental image is flatter about the axis than the simulated one. Unfortunately, lack of information on the actual shape of the laser spot does not allow one to ascertain the origin of this discrepancy. In Fig. 6, as well as in all following figures, the origin of the z axis coincides with the base of the cylinder or the base of the hemisphere; see the dashed vertical lines in Fig. 2.

In the same experiment, the transit time of the shock wave through the plastic and molybdenum layers was measured by SOP, observing the visible light emitted from the rear surface of the molybdenum layer. The shock was found to break out at time $t_{bo} = 8.5$ ns.

A more quantitative comparison between experiment and simulation is shown in Fig. 7, referring to the x-ray transmission along the symmetry axis. We find that the simulated curve, shifted by 7 μm to the left, overlaps the experimental one within experimental errors.

In the previous synthetic radiographs we assumed a x-ray Gaussian source with a 30-μm FWHM. In Fig. 8 we show how the source size affects transmission. It can be seen that the curves differ sensibly in correspondence with the shock

front. Full widths at half maximum in the range 20–40 μm are roughly consistent with experimental data.

On the basis of the good agreement between the experimental and the simulated data, we can estimate several quantities using the detailed information (such as maps of density, electron, and ion temperature and pressure) provided by the numerical simulation. In Figs. 9(a)–9(c) we show the density
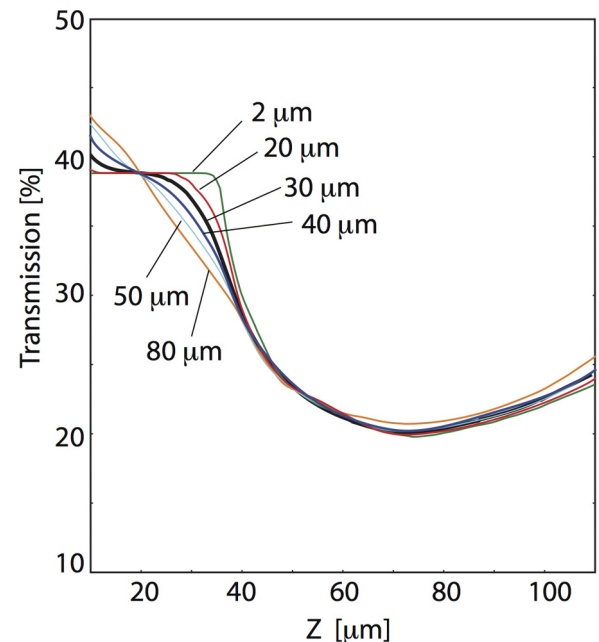

FIG. 8. Cylindrical target. Simulated transmission for different dimensions of the x-ray source. The labels in the figure refer to the source FWHM. The black curve is the same as in Fig. 7.
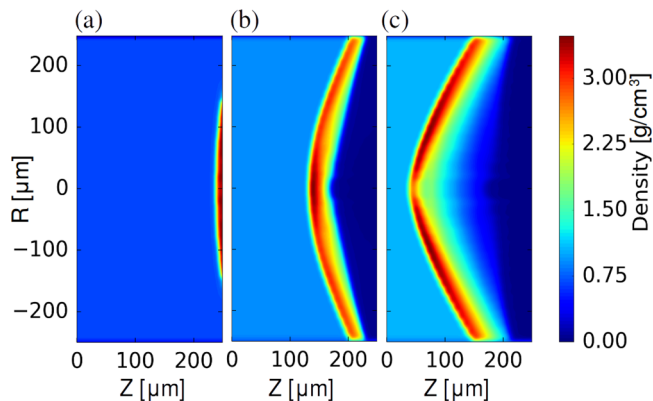
FIG. 9. Cylindrical target. Simulated density maps at times (a) $t = 0.7$ ns, (b) $t = 2.7$ ns, and (c) $t = 4.7$ ns.

maps at times $t = 0.7, 2.7$, and 4.7 ns, respectively. The density map at $t = 4.7$ ns is the same used in the synthetic radiograph and in the Abel transform. We notice how the shape of the focal spot affects the shock front. At $t = 0.7$ ns the shock front has the same radial extension as the laser focal spot. At $t = 2.7$ ns it is still flat in the center but curved at the edges. Finally, at $t = 4.7$ ns we observe a curved shock front similar to the experimental one.

It is also worth noticing that the shock break-out time from the DUED simulation, $t_{bo} \simeq 8.4$ ns, agrees with the experimental value. From the simulation we can also infer the shock pressure from the hydrodynamic simulations. The highest pressure inferred is 20 Mbars (with a density ratio between the shocked and unshocked material of about 3.8) at the end of the laser pulse at $t = 2$ ns. At $t = 4.7$ ns the inferred pressure is about 8 Mbars (with a density ratio between the shocked and unshocked material of about 3.35).

From the experimental data we could obtain directly the density map using the Abel inversion described in Sec. II C. The result is shown in Fig. 10(a). The noise of the experimental data is considerably amplified by the transformation. One simple way to improve the reconstructed density map is to apply a digital filter to the experimental image to attenuate the
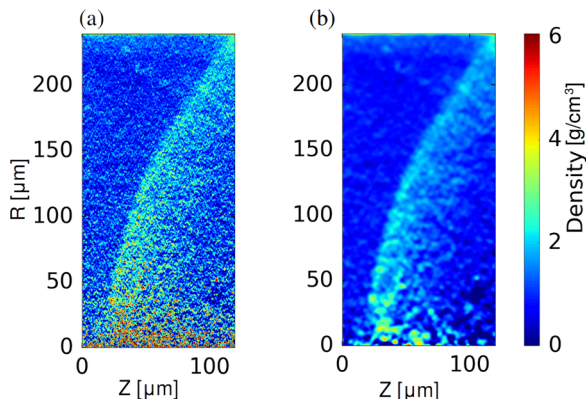

FIG. 10. Density maps from Abel inversion of the experimental radiograph shown in Fig. 6(a). (a) Abel inversion of the raw data and (b) Abel inversion applied after a Gaussian smoothing 2 pixels in radius of the raw data.
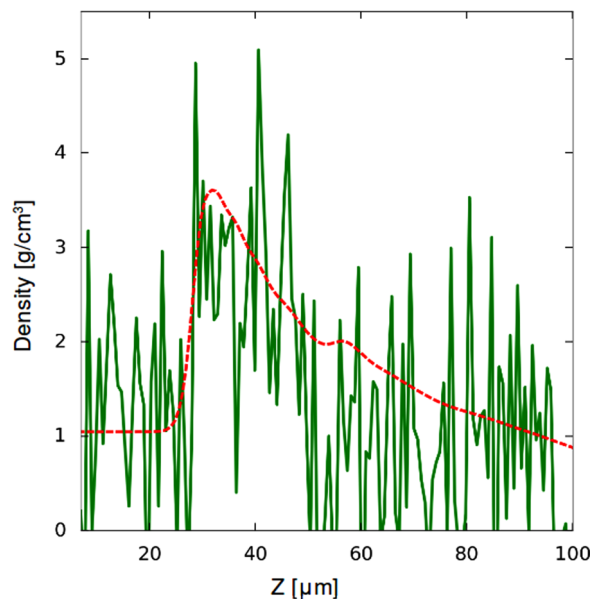

FIG. 11. Density profile along the line $r = 40\ \mu$m: Abel transform of the raw experimental data (green curve) vs DUED simulation, shifted 7 μm to the left (red dashed curve).

noise. In Fig. 10(b) we show the map obtained using a Gaussian filter two pixels in radius on the experimental data before the Abel inversion. However, once we filter data, we have a loss of information. In particular, the sharp features of the shock front are lost, hindering the possibility to measure the compression ratio and hence the strength of the shock wave. The above features are confirmed by Figs. 11 and 12, comparing density
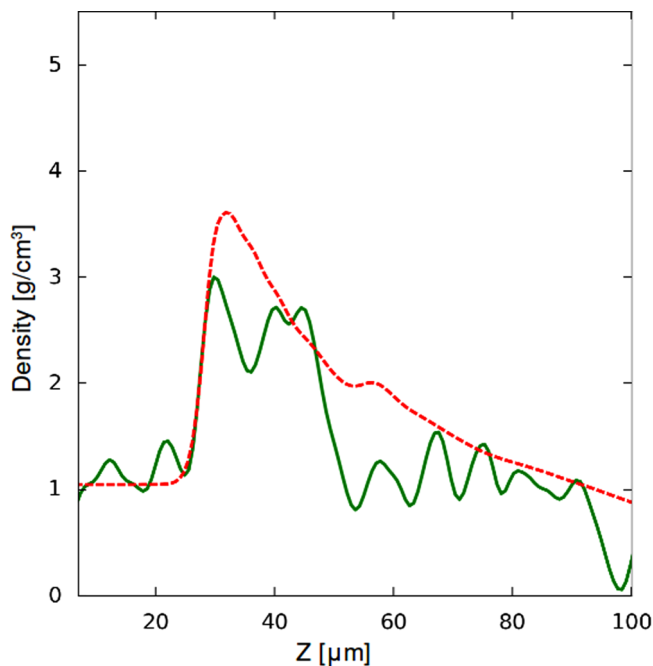

FIG. 12. Density profile along the line $r = 40\ \mu$m. Abel transform of the filtered experimental data (green curve) vs DUED simulation, shifted 7 μm to the left (red dashed curve).
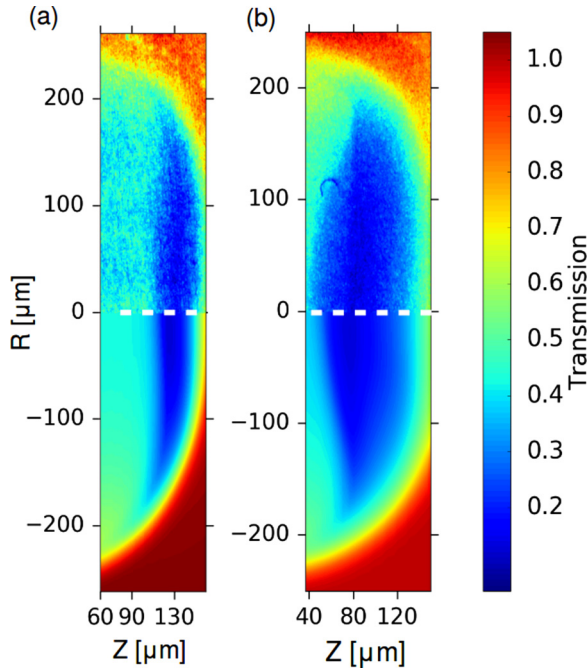
FIG. 13. Experimental radiographs (top) and synthetic radiographs (bottom) for the hemispherical target. The shock wavefront appears (a) quite flat at 2.7 ns and (b) definitely curved at 4.7 ns.

profiles along the line $r = 40\ \mu$m from Abel inversion and from DUED simulations.

B. Hemispherical target

With the hemispherical target, we acquired radiographs in two shots. In the first one (with laser energy $E_L = 450$ J) we
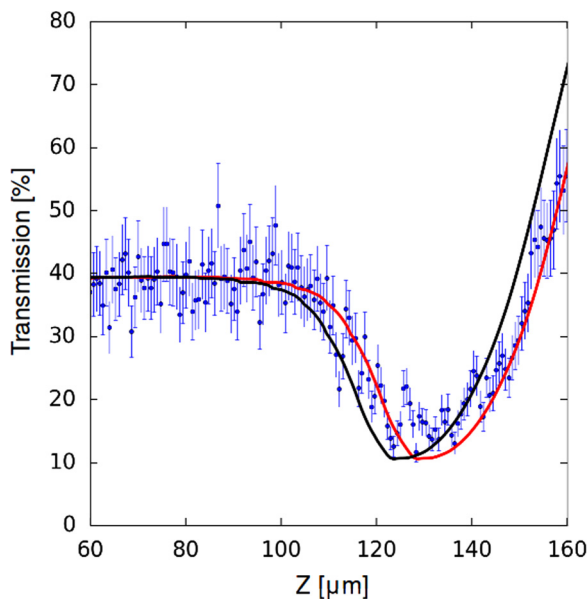

FIG. 14. Hemispherical target. Experimental transmission (dots) and simulated transmission (black curve) at $t = 2.7$ ns. The red curve is the simulated transmission curve shifted 5 μm to the right.

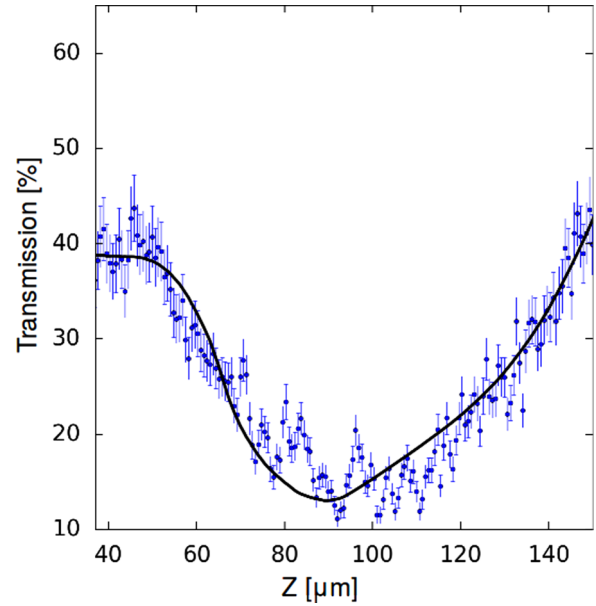FIG. 15. Same as Fig. 14, at time $t = 4.7$ ns.

acquired a radiograph at time $t = 2.7$ ns; in the second one ($E_L = 350$ J) we acquired a radiograph at $t = 4.7$ ns.

In Fig. 13 we show experimental (top) and simulated data (bottom). In the experiment, 3D effects were caused by laser mispointing. As already mentioned, to perform our analysis, we slightly rotated ($\approx 3°$) both images. In the simulations we assumed a Gaussian focal spot with a 200-μm FWHM. In both cases the laser energy was reduced to 80% of the measured value, while the power time dependence followed the experimental curve. (Using the measured value, we obtained shock velocities 6%–7% larger than the experimental ones.) Figure 13(a) shows a quite flat shock front at $t = 2.7$ ns, while Fig. 13(b) shows a curved shock front at $t = 4.7$ ns.

Experimental and simulated transmission profiles along the propagation axis at times $t = 2.7$ ns and $t = 4.7$ ns are presented in Figs. 14 and 15, respectively. The simulated curves overlap the experimental ones within experimental
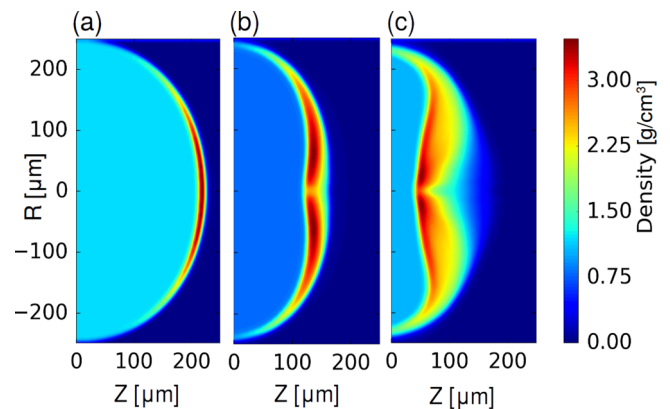

FIG. 16. DUED simulation of the hemispherical target, showing simulated density maps at three selected times: (a) $t = 0.7$ ns, (b) $t = 2.7$ ns, and (c) $t = 4.7$ ns.

errors. In the case of radiograph at $t = 2.7$ ns, better agreement is found by shifting the simulated curve by 5 μm to the right.

As we already did for the cylindrical target, also for the hemispherical target we can understand the evolution of the shock wave using the simulations. DUED simulation results are shown in Fig. 16, for a case with laser energy $E_L = 280$ J. The simulation allows us to estimate the time interval during which the shock front is almost flat. In fact, the radiographs show a nearly flat front at $t = 2.7$ ns and a curved front at $t = 4.7$ ns. According to the simulation the shock front appears nearly flat in the time interval $t = 1.7-3.5$ ns.

IV. CONCLUSION

We presented experimental results on the generation of strong shock waves, using targets with flat and hemispherical interaction surfaces. The aim was to show that, performing a proper treatment of the experimental raw data, x-ray radiography can provide valuable information concerning the shape of the shock front and, under certain conditions, the density map of the shocked target region. Experimental radiographs were favorably compared with synthetic radiographs using data generated by DUED simulations. A quantitative comparison, however, requires that a detailed knowledge of the actual laser intensity distribution in the focal spot is included in the code.

[1] R. J. Trainor, J. W. Shaner, J. M. Auerbach, and N. C. Holmes, Phys. Rev. Lett. **42**, 1154 (1979).

[2] A. Benuzzi, T. Löwer, M. Koenig, B. Faral, D. Batani, D. Beretta, C. Danson, and D. Pepler, Phys. Rev. E **54**, 2162 (1996).

[3] D. Batani, L. Antonelli, S. Atzeni, J. Badziak, F. Baffigi, T. Chodukowski, F. Consoli, G. Cristoforetti, R. De Angelis, R. Dudzak *et al.*, Phys. Plasmas **21**, 032710 (2014).

[4] R. Nora, W. Theobald, R. Betti, F. J. Marshall, D. T. Michel, W. Seka, B. Yaakobi, M. Lafon, C. Stoeckl, J. Delettrez *et al.*, Phys. Rev. Lett. **114**, 045001 (2015).

[5] D. Batani, Europhys. Lett. **114**, 65001 (2016).

[6] M. Koenig, A. B. Mounaix, A. Ravasio, T. Vinci, N. Ozaki, S. Lepape, D. Batani, G. Huser, T. Hall, D. Hicks *et al.*, Plasma Phys. Controlled Fusion **47**, B441 (2005).

[7] G. W. Collins, L. B. Da Silva, P. Celliers, D. M. Gold, M. E. Foord, R. J. Wallace, A. Ng, S. V. Weber, K. S. Budil, and R. Cauble, Science **281**, 1178 (1998).

[8] M. K. Matzen, M. A. Sweeney, R. G. Adams, J. R. Asay, J. E. Bailey, G. R. Bennett, D. E. Bliss, D. D. Bloomquist, T. A. Brunner, R. B. Campbell *et al.*, Phys. Plasmas **12**, 055503 (2005).

[9] A. Benuzzi-Mounaix, M. Koenig, A. Ravasio, T. Vinci, N. Ozaki, M. R. le Gloahec, B. Loupias, G. Huser, E. Henry, S. Bouquet *et al.*, Plasma Phys. Controlled Fusion **48**, B347 (2006).

[10] A. Ravasio, M. Koenig, S. Le Pape, A. Benuzzi-Mounaix, H. Park, C. Cecchetti, P. Patel, A. Schiavi, N. Ozaki, A. Mackinnon *et al.*, Phys. Plasmas **15**, 060701 (2008).

[11] A. B. Mounaix, B. Loupias, M. Koenig, A. Ravasio, N. Ozaki, M. R. Le Gloahec, T. Vinci, Y. Aglitskiy, A. Faenov, T. Pikuz *et al.*, Phys. Rev. E **77**, 045402 (2008).

[12] E. Brambrink, H. G. Wei, B. Barbrel, P. Audebert, A. Benuzzi-Mounaix, T. Boehly, T. Endo, C. D. Gregory, T. Kimura, R. Kodama *et al.*, Phys. Rev. E **80**, 056407 (2009).

[13] A. Morace, L. Fedeli, D. Batani, S. Baton, F. N. Beg, S. Hulin, L. C. Jarrot, A. Margarit, M. Nakai, P. Nakatsutsumi, P. Nicolai,

N. Piovella, M. S. Wei, X. Vaisseau, L. Volpe, and J. J. Santos, Phys. Plasmas **21**, 102712 (2014).

[14] S. X. Hu, V. A. Smalyuk, V. N. Goncharov, J. P. Knauer, P. B. Radha, I. V. Igumenshchev, J. A. Marozas, C. Stoeckl, B. Yaakobi, D. Shvarts, T. C. Sangster, P. W. McKenty, D. D. Meyerhofer, S. Skupsky, and R. L. McCrory, Phys. Rev. Lett. **100**, 185003 (2008).

[15] S. Le Pape, A. Macphee, D. Hey, P. Patel, A. Mackinnon, M. Key, J. Pasley, M. Wei, S. Chen, T. Ma, F. Beg, N. Alexander, R. Stephens, D. Offerman, A. Link, L. Van-Woerkom, and R. Freeman, Rev. Sci. Instrum. **79**, 106104 (2008).

[16] D. G. Hicks, B. K. Spears, D. G. Braun, R. E. Olson, C. M. Sorce, P. M. Celliers, G. W. Collins, and O. L. Landen, Rev. Sci. Instrum. **81**, 10E304 (2010).

[17] A. L. Kritcher, T. Döppner, D. Swift, J. Hawreliak, G. Collins, J. Nilsen, B. Bachmann, E. Dewald, D. Strozzi, S. Felker, O. N. Landen, O. Jones, C. Thomas, J. Hammer, C. Keane, H. J. Lee, S. H. Glenzer, S. Rothman, D. Chapman, D. Kraus, P. Neumayer, and R. W. Falcone, High Energy Density Phys. **10**, 27 (2014).

[18] S. Atzeni, A. Schiavi, F. Califano, F. Cattani, F. Cornolti, D. Del Sarto, T. Liseykina, A. Macchi, and F. Pegoraro, Comput. Phys. Commun. **169**, 153 (2005).

[19] L. M. Barker and R. E. Hollenbach, J. Appl. Phys. **43**, 4669 (1972).

[20] L. von Hámos, Naturwissenschaften **20**, 705 (1932).

[21] L. von Hámos, Ann. Phys. (Leipzig) **409**, 716 (1933).

[22] F. J. Marshall, P. W. McKenty, J. A. Delettrez, R. Epstein, J. P. Knauer, V. A. Smalyuk, J. A. Frenje, C. K. Li, R. D. Petrasso, F. H. Séguin *et al.*, Phys. Rev. Lett. **102**, 185004 (2009).

[23] J. H. Hubbell and S. M. Seltzer, Tables of x-ray mass attenuation coefficients and mass energy-absorption coefficients 1 keV to 20 MeV for elements $Z = 1$ to 92 and 48 additional substances of dosimetric interest, National Institute of Standards and Technology Report No. NISTIR 5632, 1995 (unpublished).

[24] S. Atzeni, A. Caruso, and V. Pais, Laser Part. Beams **4**, 393 (1986).

[25] M. A. Barrios, D. G. Hicks, T. R. Boehly, D. E. Fratanduono, J. H. Eggert, P. M. Celliers, G. W. Collins, and D. Meyerhofer, Phys. Plasmas **17**, 056307 (2010).

[26] K. Eidmann, Laser Part. Beams **12**, 223 (1994).

[27] R. B. Stephens, R. A. Snavely, Y. Aglitskiy, F. Amiranoff, C. Andersen, D. Batani, S. D. Baton, T. Cowan, R. R. Freeman, T. Hall, S. P. Hatchett, J. M. Hill, M. H. Key, J. A. King, J. A. Koch, M. Koenig, A. J. MacKinnon, K. L. Lancaster, E. Martinolli, P. Norreys, E. Perelli-Cippo, M. Rabec Le Gloahec, C. Rousseaux, J. J. Santos, and F. Scianitti, Phys. Rev. E **69**, 066414 (2004).